

Ellen Kuhl · Daniel W. Schmid

Computational modeling of mineral unmixing and growth

An application of the Cahn–Hilliard equation

Received: 25 November 2005/Accepted: 16 January 2006 / Published online: 21 February 2006
© Springer-Verlag 2006

Abstract A new finite element based simulation technique for mineral growth governed by the classical Cahn–Hilliard equation is presented. The particular format of the underlying Flory–Huggins free energy for non-ideal mixtures is characterized through a double-well potential. It allows for uphill diffusion driven by gradients in the chemical potential and thus provides the appropriate framework to simulate phase separation typically encountered in mineral unmixing and growth. For the finite element discretization, the governing fourth order diffusion equation is reformulated in terms of a system of two coupled second order equations. For the temporal discretization, a heuristic adaptive time stepping scheme is applied in order to simulate not only the early stages of phase separation but also the long term behavior of ageing and grain fusion. The basic features of the Cahn–Hilliard equation are elaborated by means of selected geologically relevant examples. In particular, isotropic and anisotropic mineral growth and symplectite formation are studied and the long term response in the sense of Ostwald ripening is illustrated.

Keywords Fourth order diffusion · Surface tension · Finite element method · Spinodal decomposition · Geomechanics

1 Motivation

Most rocks and minerals found at or near the earth surface have a complex history and were formed at completely different pressure and temperature conditions than those that prevail at the surface of our planet. Minerals that form solid solutions may, under certain conditions, adjust to the lowered temperatures by unmixing or exsolution [21]. The resulting

textures are often spectacular intergrowth patterns of minerals that grew simultaneously at the location where the host mineral became thermodynamically unstable, illustrated in Fig. 1. Since solid solution minerals are quite abundant exsolution textures can be found frequently in rocks from the earth, moon [11], mars [1], and in many iron meteorites, e.g. Widmanstätten figures [21]. A related phenomenon to mineral exsolution is symplectitic growth, which yields similar intergrowth pattern. In contrast to mineral exsolution, which is a solid-state process in a closed system, symplectites may involve fluids and small amounts of residual magma in an open system [25].

The patterns and chemical compositions of mineral exsolution and symplectites potentially contain crucial information for the reconstruction of the geological history of an outcrop or region. However, this geological history reconstruction can only be performed if adequate quantitative tools are available. We propose to exploit the similarity between mineral exsolution to related processes in alloys and polymers where homogeneous mixtures undergo phase separation, also called spinodal decomposition, when thrust into a two-phase region by, for example, a thermal quench (cf. Fig. 2). Obviously, the underlying process of phase separation requires uphill diffusion in which material moves against concentration gradients. Accordingly, the classical Fickian diffusion equation which tends to generate uniform concentration profiles is no longer applicable. An appropriate framework in which phase separation is driven by gradients in the chemical potential rather than by concentration gradients is provided by Flory–Huggins thermodynamics of mixing, see, e.g., Flory [6] and Huggins [10]. The corresponding nonlinear diffusion equation can correctly predict phase separation on a material point level, however, it fails to predict the kinetics and morphology evolution of phase separation in large systems. To remedy this deficiency, the concept of gradient energy can be introduced via the Landau-Ginzburg functional. The resulting governing fourth order diffusion equation is typically attributed to Cahn [3] and Cahn and Hilliard [4, 5] although the basic ideas of a surface energy can already be found in the earlier work of van der Waals [27].

E. Kuhl (✉)
Chair of Applied Mechanics, TU Kaiserslautern,
D-67653, Kaiserslautern, Germany
E-mail: ekuhl@rhrk.uni-kl.de

D. W. Schmid
Physics of Geological Processes,
University of Oslo, N-0316, Oslo, Norway
E-mail: d.w.schmid@fys.uio.no

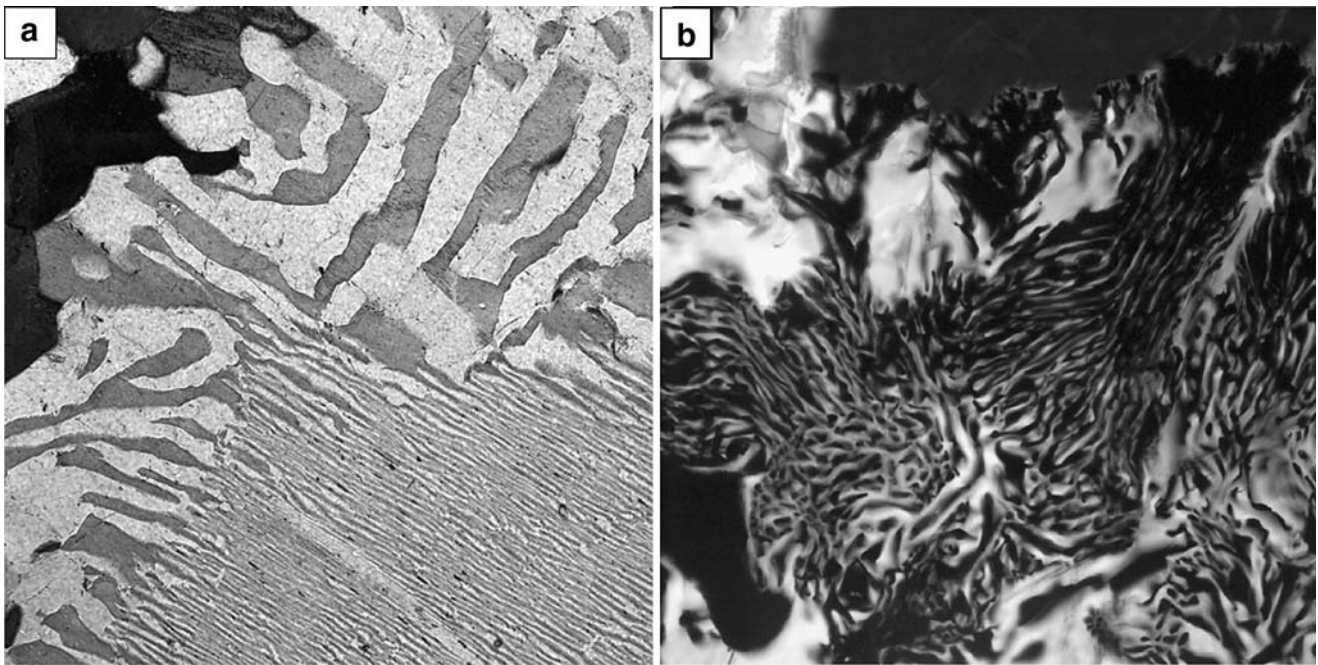


Fig. 1 Examples of **a** mineral exsolution (perthite, i.e. alkali-feldspar unmixing) and **b** symplectite (garnet finger print texture). Field of view in both examples ca. 1 mm

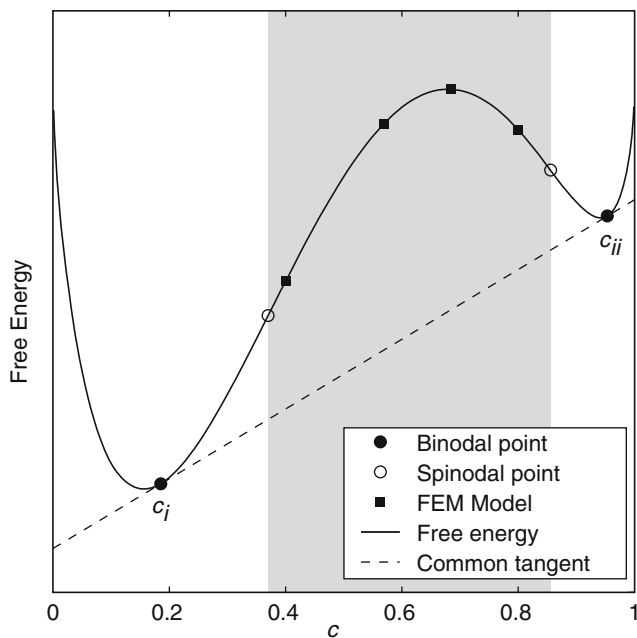


Fig. 2 Double well shaped configurational energy. The spinodal region, where spontaneous phase separation takes place, is underlain in gray. The particular curve is calculated for an alkali-feldspar solid solution at 6000 bar and 800 K, taken from Waldbaum and Thompson [29]. Note, that the c is given here in terms of albite

An excellent overview on nonlinear diffusion and phase separation was presented recently by Nauman and He [18], see also Gurtin [8] and Novick-Cohen and Segel [19].

The Cahn–Hilliard equation governs the initial exsolution process, where phase separation is controlled by the local configurational energy, as well as later-stage domain coarsen-

ing driven by the reduction of the total interfacial free energy. It was shown by Langer [12] that this coarsening is equivalent to Ostwald ripening [20] where the domain size grows proportional to the third root of time as derived by Lifshitz and Slyozov [15] and Wagner [28]. Ostwald ripening involves larger ones, or, in the case of coarse grained intergrowth, the solid-state grain boundary migration driven by locally high interfacial energies. Exsolution textures in minerals follow this two step process. The first phase of unmixing leads to sinusoidal perturbations [7] that are then amplified, followed by Ostwald ripening with the described domain growth law [16].

As shown in Fig. 1a exsolution textures are frequently anisotropic. We investigate this by studying the effect of anisotropic diffusion coefficients. Another important parameter may be strain. However, the often random arrangement of the delicate exsolution and symplectite textures (cf. Fig. 1b) suggests that they typically grow in low-strain locations, see, e.g., Vernon [25]. Nevertheless, strain may contribute directly to their formation through the effect of strain energy on the total free energy [23], or indirectly as the textures may become distorted and recrystallized into granular aggregates when being subjected to strain. Based on our current research and anticipating future research along the lines of Asaro and Tiller [2] and Srolovitz [22], we shall apply a finite element based numerical simulation technique, closely related to the recent formulation by Ubachs et al. [23, 24]. This allows for the simulation of arbitrary geometries and could easily be coupled to small or possibly even large deformation calculations, see e.g. Larché and Cahn [13].

The manuscript is organized as follows: in Sect. 2 we summarize the governing equations of nonlinear nonlocal

diffusion of Cahn–Hilliard type which finally result in a governing fourth order diffusion equation. We then discuss its temporal and spatial discretization based on its partition into a set of two coupled second order equations in Sect. 3. Section 4 illustrates the basic features of the Cahn–Hilliard equation by means of selected examples. In particular, we address the influence of the internal length scale and the ability of the formulation to predict not only particulate but also co-continuous worm-like micro-structures. Long term behavior in the sense of Ostwald ripening is studied and a geologically relevant example of anisotropic mineral growth in individual crystal grains is analyzed. A final discussion and an outlook are given in Sect. 5.

2 Governing equations

In what follows, we shall briefly summarize the governing equations of nonlinear nonlocal diffusion of Cahn–Hilliard type. A typical problem of interest consists in determining the evolution of the order parameter c , which characterizes the concentration of one of the reactants as $0 \leq c \leq 1$ and which is governed by the following parabolic diffusion equation.

$$d_t c = -\nabla \cdot \mathbf{j} \quad \text{with} \quad \mathbf{j} = -\mathbf{M} \cdot \nabla \mu. \quad (1)$$

The flux of concentrations \mathbf{j} is driven by gradients in the chemical potential $\nabla \mu$ weighted by the mobility \mathbf{M} .

$$d_t c = \nabla \cdot (\mathbf{M} \cdot \nabla \mu). \quad (2)$$

Unlike the classical Fickian diffusion equation, the above equation describes a redistribution of concentrations such that chemical potential μ is uniformly distributed at equilibrium. It thus provides the appropriate framework for non-ideal mixtures encountered in mineral exsolution. The chemical potential μ can be related to the free energy Ψ

$$\mu = \delta_c \Psi \quad \Psi = \Psi^{\text{con}}(c) + \Psi^{\text{sur}}(\nabla c) \quad (3)$$

through the variational derivative $\delta_c(\bullet) = \partial_c(\bullet) - \nabla \cdot (\partial_{\nabla c}(\bullet))$ whereby $\Psi^{\text{con}} = \Psi^{\text{con}}(c)$ denotes the configurational free energy in terms of the local concentration c and $\Psi^{\text{sur}} = \Psi^{\text{sur}}(\nabla c)$ is the surface free energy which depends on the concentration gradients ∇c . Recall that if deformation is believed to have a strong influence on the unmixing process, an additional energy contribution from the elastic strain energy $\Psi^{\text{str}} = \Psi^{\text{str}}(\epsilon)$ would have to be incorporated in Eq.(3)₂. However, motivated by the experimental findings of Hovis et al. [9], we decided to neglect the elastic strain energy for the time being. Accordingly, the chemical potential takes the following explicit representation.

$$\mu = \partial_c \Psi^{\text{con}} - \nabla \cdot (\partial_{\nabla c} \Psi^{\text{sur}}). \quad (4)$$

The configurational energy Ψ^{con} and the surface energy Ψ^{sur} will be specified in the following subsections.

2.1 Configurational energy

According to the Flory–Huggins thermodynamics of mixing, the configurational free energy of a general multi-component mixture can be expressed as follows.

$$\Psi^{\text{con}} = \sum_i g_i c_i + \sum_i RT c_i \ln(c_i) + \Psi^{\text{exc}}(c_i). \quad (5)$$

In the sequel, we shall assume a two phase medium with $c_1 = c$ and $c_2 = [1 - c]$. Accordingly, the gradient of the configurational free energy defines the configurational contribution to the chemical potential

$$\mu^{\text{con}} = \partial_c \Psi^{\text{con}}, \quad (6)$$

the gradient of which reduces to the following expression.

$$\nabla \mu^{\text{con}} = \partial_c^2 \Psi^{\text{con}} \nabla c. \quad (7)$$

The first term in the configurational free energy (5) $g_1 c + g_2 [1 - c]$ represents the free energy of the individual components. The second term $RT c \ln(c) + RT [1 - c] \ln(1 - c)$ accounts for the entropy of mixing whereby T is the absolute temperature and R is the gas constant. The excess energy Ψ^{exc} accounts for the mixture being nonideal. It contains higher order terms in the concentration c weighted by Margules parameters, which are essentially responsible for the particular shape of the configurational energy. A characteristic double well potential for alkali-feldspar exsolution, based on the parameter set applied in Sect. 4, is illustrated in Fig. 2.

Provided that $\Psi^{\text{con}}(c)$ has two internal minima within the admissible region $0 \leq c \leq 1$, the two points for which $\partial_c^2 \Psi^{\text{con}}(c) = 0$ are called the spinodal points. The region between these points is the unstable spinodal region in which the effective diffusivity is negative. The two characteristic points c_i and c_{ii} external to the spinodal region and given by the common tangent condition $\partial_c \Psi^{\text{con}}(c_i) = \partial_c \Psi^{\text{con}}(c_{ii})$ are the so-called binodal points. A mixture quenched into the spinodal region will separate into two phases of the either of the two binodal compositions c_i and c_{ii} , compare Fig. 2.

2.2 Surface energy

The configurational energy of Flory–Huggins type introduced in the previous section provides the appropriate framework for spinodal decomposition in non-ideal mixtures. However, due to the lack of a surface energy term in the free energy expression, the configurational energy alone is not able to describe the process of phase separation appropriately. A related numerical simulation that is not equipped with an internal length scale will predict spuriously oscillating concentration profiles. Following Cahn and Hilliard [4, 5], we thus introduce a surface free energy of the following format.

$$\Psi^{\text{sur}} = \frac{1}{2} \nabla c \cdot \boldsymbol{\kappa} \cdot \nabla c. \quad (8)$$

Accordingly, the surface contribution to the chemical potential takes the following representation.

$$\mu^{\text{sur}} = -\nabla \cdot (\partial_{\nabla c} \Psi^{\text{sur}}) = -\nabla \cdot (\boldsymbol{\kappa} \cdot \nabla c). \quad (9)$$

With a constant isotropic gradient energy coefficient $\boldsymbol{\kappa} = \kappa \mathbf{I} = \text{const}$, the gradient of the surface contribution to the chemical potential can be expressed in the following form.

$$\nabla \mu^{\text{sur}} = -\boldsymbol{\kappa} \cdot \nabla (\Delta c). \quad (10)$$

Recall that the gradient energy coefficient κ has the dimension of energy times a length squared and thus introduces a regularizing internal length scale into the formulation.

2.3 Fourth order diffusion equation

Following the previous subsections, mineral exsolution and growth is characterized by a fourth order equation in terms of the concentration c .

$$d_t c = \nabla \cdot (\mathbf{M} \cdot [\partial_c^2 \Psi^{\text{con}} \nabla c - \kappa \cdot \nabla (\nabla \cdot (\nabla c))]). \quad (11)$$

From a technical point of view, the numerical solution of the above equation is rather cumbersome. In the context of the finite element method, its spatial discretization would require a C^1 -continuous interpolation of the concentration field c , a procedure which is well-known in the context of thin beam and plate theories where Hermitian polynomials are applied to ensure higher order continuity. Alternatively, the recently developed discontinuous Galerkin method could be applied to ensure higher order continuity, see Wells et al. (2006). To avoid these additional difficulties, we suggest the introduction of a nonlocal concentration field \bar{c} .

$$\bar{c} = c + \lambda^2 \nabla \cdot (\nabla c). \quad (12)$$

Accordingly, the surface contribution to the chemical potential $-\kappa \cdot \nabla (\nabla \cdot (\nabla c)) = \gamma \nabla c - \gamma \nabla \bar{c}$ can be expressed in terms of the local concentration field c and its nonlocal counterpart \bar{c} . The single fourth order equation (11) can thus be replaced by the following set of two coupled second order equations

$$\begin{aligned} d_t c &= \nabla \cdot (\mathbf{M} \cdot [[\partial_c^2 \Psi^{\text{con}} + \gamma] \nabla c - \gamma \nabla \bar{c}]), \\ \bar{c} &= c + \lambda^2 \nabla \cdot (\nabla c), \end{aligned} \quad (13)$$

whereby the gradient of the chemical potential $\nabla \mu = [\partial_c^2 \Psi^{\text{con}} + \gamma] \nabla c - \gamma \nabla \bar{c}$ is finally a first order gradient in terms of the primary unknowns c and \bar{c} . The gradient energy coefficient $\kappa = \gamma \lambda^2$ can then be understood as the product of the energy γ , times an internal length λ , squared. At this point, the multiplicative decomposition of κ seems rather arbitrary since it is obviously non-unique. In the numerical examples presented later on, however, the choice of γ and λ is primarily driven by the aim of keeping the condition number of the final system of equations in a reasonable range.

Note that instead of introducing the dimensionless nonlocal concentration $\bar{c} = c + \lambda^2 \nabla \cdot (\nabla c)$, we could equally well have introduced the chemical potential μ or the second order gradient $\nabla \cdot (\nabla c)$ as the second independent variable. However, for the sake of conditioning of the resulting iteration matrices, we prefer the discretization of the nonlocal concentration field \bar{c} which is of the same order of magnitude as the local concentration c .

Remark 1 (Analogy to beam theories) Conceptionally speaking, the fourth order diffusion equation (11) can be compared to the classical fourth order equation $EI w^{IV} = -q$ of the Euler–Bernoulli beam theory. It is well-known that in the finite

element context, this equation would also require a C^1 continuous interpolation of the deflection w . The Euler–Bernoulli beam theory can be understood as a special case of the Timoshenko beam theory based on two second order equations $EI \Psi'' = Q$ and $GA[w'' + \Psi'] = -q$ whereby the shear stiffness GA tends to infinity. In our formulation, the interface energy per unit surface γ and the internal length λ remain of finite value. Accordingly, we did not encounter typical locking problems characteristic for the thin- or thick-beam regime.

Remark 2 (Constant vs. concentration dependent mobility) In the simplest case, we could assume a constant mobility which is then equivalent to the diffusivity \mathbf{D} .

$$\mathbf{M} = \mathbf{D}. \quad (14)$$

Thermodynamic reasoning, however, suggests the choice of

$$\mathbf{M} = c [1 - c] \mathbf{D} / RT, \quad (15)$$

which, as we will see later, results in Fickian diffusion in the case of ideal solution.

Remark 3 (Isotropic vs. anisotropic diffusion) In the case of isotropic mineral growth, the diffusivity tensor \mathbf{D} can be expressed in terms of the identity tensor weighted by the scalar valued diffusion coefficient D .

$$\mathbf{D} = D \mathbf{I}. \quad (16)$$

An anisotropic diffusion process, motivated by the orientation of the crystallographic lattice, can be described by incorporating the structural tensor $\mathbf{n} \otimes \mathbf{n}$, where \mathbf{n} is the characteristic direction. This introduces the following format,

$$\mathbf{D} = D^{\text{iso}} \mathbf{I} + D^{\text{ani}} \mathbf{n} \otimes \mathbf{n} \quad (17)$$

in terms of the scalar valued isotropic and anisotropic diffusion coefficients D^{iso} and D^{ani} . The influence of anisotropic diffusion in the context of mineral growth will be illustrated in Sect. 4.4.

Remark 4 (Special case of Fickian diffusion) For the particular parameter set of $\psi^{\text{exc}} = 0$ or the end-member cases $c = 0$ and $c = 1$ the above formulation reduces to the classical case of linear Fickian diffusion. In this special case, the flux of concentrations \mathbf{j} is driven by gradients in the concentration ∇c , i.e. $\mathbf{j} = -\mathbf{D} \cdot \nabla c$ and thus

$$d_t c = \nabla \cdot (\mathbf{D} \cdot \nabla c). \quad (18)$$

In contrast to the general diffusion of Cahn–Hilliard type, classical Fickian diffusion predicts the generation of uniform concentration profiles at equilibrium. Fickian diffusion is thus strictly limited to an ideal mixture that has somehow become inhomogeneous.

3 Discretization

In what follows we shall elaborate the temporal and spatial discretization of the nonlinear set of coupled governing Eqs. (13) which can be cast into the following residual statements

$$\begin{aligned} \mathbf{R}^c &= d_t c - \nabla \cdot (\mathbf{M} \cdot \nabla \mu) \doteq 0 \quad \text{in } \mathcal{B}, \\ \mathbf{R}^{\bar{c}} &= \bar{c} - c - \lambda^2 \nabla \cdot (\nabla c) \doteq 0 \quad \text{in } \mathcal{B}, \end{aligned} \quad (19)$$

with the residuals of the diffusion problem \mathbf{R}^c and of the non-local problem $\mathbf{R}^{\bar{c}}$ being functions of the primary unknowns c and \bar{c} . Next, the boundary $\partial\mathcal{B}$ of the domain of interest is decomposed into disjoint parts $\partial\mathcal{B}_c$ and $\partial\mathcal{B}_q$ for the diffusion problem and into $\partial\mathcal{B}_{\bar{c}}$ and $\partial\mathcal{B}_{\bar{q}}$ for the nonlocal problem, respectively. While Dirichlet boundary conditions are prescribed on $\partial\mathcal{B}_c$ and $\partial\mathcal{B}_{\bar{c}}$, Neumann boundary conditions can be given for the chemical potential and for the concentration flux on $\partial\mathcal{B}_q$ and $\partial\mathcal{B}_{\bar{q}}$,

$$\begin{aligned} c &= c^p \quad \text{on } \partial\mathcal{B}_c \quad \nabla \mu \cdot \mathbf{n} = q^p \quad \text{on } \partial\mathcal{B}_q \\ \bar{c} &= \bar{c}^p \quad \text{on } \partial\mathcal{B}_{\bar{c}} \quad \nabla \bar{c} \cdot \mathbf{n} = \bar{q}^p \quad \text{on } \partial\mathcal{B}_{\bar{q}} \end{aligned} \quad (20)$$

with \mathbf{n} denoting the outward normal to $\partial\mathcal{B}$. The corresponding weak forms \mathbf{G}^c and $\mathbf{G}^{\bar{c}}$ follow straightforwardly by multiplying the residual statements (19) and the Neumann boundary conditions (20) with the corresponding test functions $w, \bar{w} \in H_1^0(\mathcal{B})$.

$$\begin{aligned} \mathbf{G}^c &= \int_{\mathcal{B}} w \, d_t c + \nabla w \cdot \mathbf{M} \cdot \nabla \mu \, dv - \int_{\partial\mathcal{B}_q} w \, q^p \, da \doteq 0, \\ \mathbf{G}^{\bar{c}} &= \int_{\mathcal{B}} \bar{w} [\bar{c} - c] + \nabla \bar{w} \cdot \lambda^2 \nabla c \, dv - \int_{\partial\mathcal{B}_{\bar{q}}} \bar{w} \, \bar{q}^p \, da \doteq 0. \end{aligned} \quad (21)$$

Following the original thermodynamic derivation by Cahn and Hilliard [4, 5], we prescribe homogeneous Neumann boundary conditions for the concentration flux to ensure the conservation of concentrations. In addition, we shall also apply homogeneous Neumann boundary conditions for the flux of the chemical potential in the sequel.

3.1 Temporal discretization

For the temporal discretization we partition the time interval of interest \mathcal{T} into n_{stp} subintervals $[t_n, t_{n+1}]$ as

$$\mathcal{T} = \bigcup_{n=0}^{n_{\text{stp}}-1} [t_n, t_{n+1}], \quad (22)$$

and focus on a typical time slab $[t_n, t_{n+1}]$. Let us denote the current time increment by $\Delta t := t_{n+1} - t_n > 0$ and assume that the local and nonlocal concentration c_n and \bar{c}_n and all derivable quantities are known at the beginning of the actual subinterval t_n . In the spirit of a one parameter family of implicit time marching schemes, we shall evaluate the set of governing equations at time $t_{n+\theta}$, whereby $0 \leq \theta \leq 1$.

In combination with the following finite difference approximation of the first order time derivative $d_t c$ as

$$d_t c = \frac{1}{\Delta t} [c_{n+1} - c_n], \quad (23)$$

we obtain the following semi-discrete weak forms

$$\begin{aligned} \mathbf{G}_{n+\theta}^c &= \int_{\mathcal{B}} w \frac{c_{n+1} - c_n}{\Delta t} + \nabla w \cdot \mathbf{M}_{n+\theta} \cdot \nabla \mu_{n+\theta} \, dv \\ &\quad - \int_{\partial\mathcal{B}_q} w \, q_{n+\theta}^p \, da, \\ \mathbf{G}_{n+\theta}^{\bar{c}} &= \int_{\mathcal{B}} \bar{w} [\bar{c}_{n+\theta} - c_{n+\theta}] + \nabla \bar{w} \cdot \lambda^2 \nabla c_{n+\theta} \, dv \\ &\quad - \int_{\partial\mathcal{B}_{\bar{q}}} \bar{w} \, \bar{q}_{n+\theta}^p \, da. \end{aligned} \quad (24)$$

with $\{\bullet\}_{n+\theta}$ denoting values at $t_{n+\theta}$ which can be interpolated as $\{\bullet\}_{n+\theta} = [1 - \theta] \{\bullet\}_n + \theta \{\bullet\}_{n+1}$.

Remark 5 (Special cases of time integration schemes) The proposed one parameter family of time integration schemes includes the classical implicit Euler backward scheme for $\theta = 1.0$, the implicit Crank–Nicholson scheme for $\theta = 0.5$ and an explicit time integration scheme for $\theta = 0.0$ as special cases. However, the variation of the time integration parameter $0 < \theta \leq 1$ carried out for the different examples in Sect. 4 did not reveal a significant sensitivity with respect to the choice of time integration scheme.

3.2 Spatial discretization

In contrast to most existing nonlinear fourth order diffusion simulations in the literature, which apply either spectral methods or finite difference schemes, we suggest a finite element based discretization strategy which allows for the numerical analysis of arbitrarily shaped domains. Moreover, since we aim at coupling the formulation to deformation problems in the future, a finite element discretization appears to be a natural choice. Hence, we partition the domain of interest into n_{el} elements

$$\mathcal{B} = \bigcup_{e=1}^{n_{\text{el}}} \mathcal{B}^e \quad (25)$$

and adopt an elementwise interpolation of the test functions w and \bar{w} and the trial functions c and \bar{c} .

$$\begin{aligned} w &= \sum_{i=1}^{n_{\text{en}}} N_i w^i & \bar{w} &= \sum_{j=1}^{n_{\text{en}}} N_j \bar{w}^j \\ c &= \sum_{k=1}^{n_{\text{en}}} N_k c^k & \bar{c} &= \sum_{l=1}^{n_{\text{en}}} N_l \bar{c}^l \end{aligned} \quad (26)$$

with n_{en} denoting the number of element nodes and N being the nodal shape functions over \mathcal{B}^e . In principle, these can be chosen independently for the interpolation of the individual test and trial functions. The discrete residuals of diffusion equation and nonlocal equation then take the following format

$$\begin{aligned} \mathbf{R}_I^c &= \mathbf{A}_{e=1}^{n_{el}} \int_{\mathcal{B}^e} N_i \frac{c_{n+1} - c_n}{\Delta t} + \nabla N_i \cdot \mathbf{M} \cdot \nabla \mu \, dv + \int_{\partial \mathcal{B}_q^e} N_i q^p \, da \\ \mathbf{R}_J^{\bar{c}} &= \mathbf{A}_{e=1}^{n_{el}} \int_{\mathcal{B}^e} N_j [\bar{c} - c] + \nabla N_j \cdot \lambda^2 \nabla c \, dv + \int_{\partial \mathcal{B}_q^e} N_j \bar{q}^p \, da \end{aligned} \quad (27)$$

wherein $\mathbf{A}_{e=1}^{n_{el}}$ denotes the assembly of the element residuals at the individual element nodes $i, j = 1, \dots, n_{en}$ to the global nodes $I, J = 1, \dots, n_{np}$. Note that the indices $\{\bullet\}_{n+\theta}$ have been omitted for the sake of transparency.

3.3 Linearization

The discrete residual statements (27) represent a highly non-linear coupled system of equations. We therefore suggest an incremental iterative monolithical solution strategy based on the classical Newton Raphson scheme. To this end, we carry out a linearization of the governing equations

$$\begin{aligned} \mathbf{R}_{I \, n+1}^c &= \mathbf{R}_{I \, n+1}^{c \, k} + d \mathbf{R}_I^c \doteq 0, \\ \mathbf{R}_{J \, n+1}^{\bar{c}} &= \mathbf{R}_{J \, n+1}^{\bar{c} \, k} + d \mathbf{R}_J^{\bar{c}} \doteq 0, \end{aligned} \quad (28)$$

where $d\mathbf{R}_I^c$ and $d\mathbf{R}_J^{\bar{c}}$ denote the incremental residuals. They can be expressed as follows

$$\begin{aligned} d\mathbf{R}_I^c &= \sum_{K=1}^{n_{np}} \mathbf{K}_{IK}^{cc} \cdot dc_K + \sum_{L=1}^{n_{np}} \mathbf{K}_{IL}^{c\bar{c}} \, d\bar{c}_L \\ d\mathbf{R}_J^{\bar{c}} &= \sum_{K=1}^{n_{np}} \mathbf{K}_{JK}^{\bar{c}c} \cdot dc_K + \sum_{L=1}^{n_{np}} \mathbf{K}_{JL}^{\bar{c}\bar{c}} \, d\bar{c}_L \end{aligned} \quad (29)$$

in terms of the following iteration matrices

$$\begin{aligned} \mathbf{K}_{IK}^{cc} &= \mathbf{A}_{e=1}^{n_{el}} \int_{\mathcal{B}^e} N_i \frac{1}{\Delta t} N_k \, dv \\ &+ \mathbf{A}_{e=1}^{n_{el}} \int_{\mathcal{B}^e} \nabla N_i \cdot \partial_c \mathbf{M} \cdot \nabla \mu \, N_k \, dv \\ &+ \mathbf{A}_{e=1}^{n_{el}} \int_{\mathcal{B}^e} \nabla N_i \cdot \mathbf{M} \partial_c^3 \Psi^{\text{con}} \cdot \nabla c \, N_k \, dv \\ &+ \mathbf{A}_{e=1}^{n_{el}} \int_{\mathcal{B}^e} \nabla N_i \cdot \mathbf{M} [\partial_c^2 \Psi^{\text{con}} + \gamma] \cdot \nabla N_k \, dv \quad (30) \\ \mathbf{K}_{IL}^{c\bar{c}} &= \mathbf{A}_{e=1}^{n_{el}} \int_{\mathcal{B}^e} -\nabla N_i \cdot \mathbf{M} \gamma \cdot \nabla N_l \, dv \\ \mathbf{K}_{JK}^{\bar{c}c} &= \mathbf{A}_{e=1}^{n_{el}} \int_{\mathcal{B}^e} -N_j \, N_k + \nabla N_j \cdot \lambda^2 \nabla N_c^k \, dv \\ \mathbf{K}_{JL}^{\bar{c}\bar{c}} &= \mathbf{A}_{e=1}^{n_{el}} \int_{\mathcal{B}^e} N_j \, N_l \, dv \end{aligned}$$

and yield the discrete incremental update of the nodal unknowns $c_{K \, n+1}^{k+1} = c_{K \, n+1}^k + dc_K$ and $\bar{c}_{L \, n+1}^{k+1} = \bar{c}_{L \, n+1}^k + d\bar{c}_L$.

In the context of a concentration dependent mobility of $\mathbf{M} = c[1-c]\mathbf{D}$, the linearization of the mobility tensor results in $\partial_c \mathbf{M} = [1-2c]\mathbf{D}$.

Remark 6 (Adaptive time stepping scheme) Due to the particular nature of the Cahn–Hilliard equation, an adaptive time stepping procedure is crucial, in particular when interest is focussed on the long term response in the sense of Ostwald ripening, e.g. [26]. We suggest an adaptive time marching scheme for which the time step size is continuously adjusted based on the convergence behavior of the Newton Raphson iteration. In particular, we divide the current time step size by two if more than six Newton iterations are required to reach the incremental equilibrium state whereas otherwise, we increase the time step by 10%. Although rather heuristic, this approach has proven to be extremely powerful in simulating all stages of mineral exsolution.

4 Examples: mineral exsolution and growth

We will now illustrate the basic features of the Cahn–Hilliard equation and its numerical realization in the context of mineral exsolution and growth. For the examples elaborated in the sequel, we consider an alkali-feldspar solid solution quenched into a two phase region, cf. Fig. 2. The pure phases, $c = 0$ and $c = 1$, correspond to the potassium (KAlSi_3O_8) and sodium ($\text{NaAlSi}_3\text{O}_8$) end-members, respectively. For this particular example, the configurational energy introduced in Eq. (5) can be specified as follows, see Waldbaum and Thompson [29].

$$\begin{aligned} \Psi^{\text{con}} &= g_1 c + g_2 [1-c] \\ &+ TR c \ln(c) + TR [1-c] \ln(1-c) \\ &+ \chi_1 c^2 [1-c] + \chi_2 [1-c]^2 c. \end{aligned} \quad (31)$$

Accordingly, the configurational contribution to the chemical potential $\mu^{\text{con}} = \partial_c \Psi^{\text{con}}$ takes the following explicit representation.

$$\begin{aligned} \partial_c \Psi^{\text{con}} &= g_1 - g_2 \\ &+ TR [1 + \ln(c)] + TR [-1 - \ln(1-c)] \\ &+ \chi_1 [2c - 3c^2] + \chi_2 [1 - 4c + 3c^2]. \end{aligned} \quad (32)$$

The higher order derivatives, which are the only ones needed for the calculation of the iteration matrices introduced in (30), take the following format.

$$\begin{aligned} \partial_c^2 \Psi^{\text{con}} &= \frac{TR}{c} + \frac{TR}{1-c} + \chi_1 [2-6c] + \chi_2 [-4+6c], \\ \partial_c^3 \Psi^{\text{con}} &= -\frac{TR}{c^2} + \frac{TR}{[1-c]^2} - 6\chi_1 + 6\chi_2. \end{aligned} \quad (33)$$

Hence, the following results are independent from the choice of g_1 and g_2 .

The Margules parameters χ_1 and χ_2 are typically functions of pressure and temperature. For our alkali-feldspar

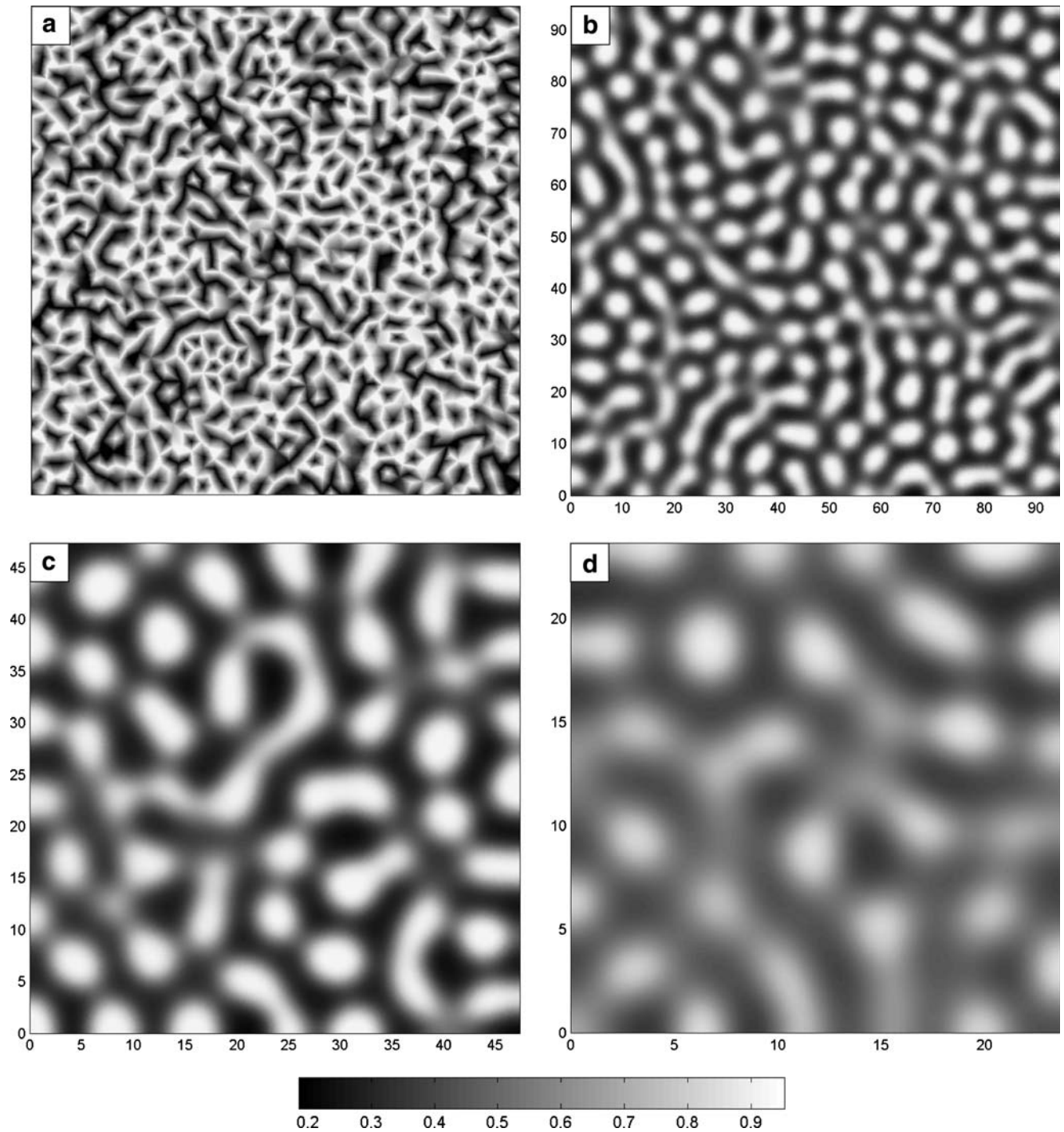


Fig. 3 Isotropic diffusion – influence of the surface energy Ψ^{surf} introduced through variations of the gradient energy parameter κ . Average system concentration is $c^{\text{ini}} = 0.57$, see Fig. 2. **a** $\kappa = 0$, consequently there is no characteristic length scale, see Eq. (35). Note, that the numerical resolution in this picture is reduced so that the mesh sensitivity is visible. **b** $\kappa = \kappa^{\text{fsp}}$, where κ^{fsp} is a realistic gradient energy for alkali-feldspars, $t^* = 36$. **c** $\kappa = 4 * \kappa^{\text{fsp}}$, $t^* = 36$. **d** $\kappa = 8 * \kappa^{\text{fsp}}$, $t^* = 36$

solid solution example, they are given by Waldbaum and Thompson [29] as follows.

$$\begin{aligned} \chi_1 &= 32098 - 16.1356 T + 0.4690 p, \\ \chi_2 &= 26470 - 19.3810 T + 0.3870 p. \end{aligned} \quad (34)$$

We assume a constant temperature of $T = 800$ K and a pressure of $p = 6000$ bar for all simulations. The gas constant is $R = 8.314$ J/mol/K.

The following examples are based on a square domain discretized by approximately 150000 unstructured triangu-

lar elements. A linear equal order interpolation is applied for the local and the nonlocal concentration field thus introducing approximately 150000 degrees of freedom. The only exception to this is Fig. 3a, where we study the mesh sensitivity. Note that a relatively fine discretization is required in order to resolve the high concentration gradients appropriately.

Throughout the calculations, we prescribe homogeneous Neumann boundary conditions, which ensure the conservation of concentrations and generate contours that are orthogonal to the boundary as the boundary is assumed to be flux free. Recall that the choice of homogeneous Neumann boundary conditions introduces a size effect. In the literature, in particular in combination with spectral methods, periodic boundary conditions are usually preferred giving a softer response in the sense of homogenization. Fortunately, the influence of the boundary vanishes upon increasing the domain size and is thus negligible for sufficiently large domains as analysed in the sequel.

In order to introduce slight initial inhomogeneities, the initial concentration c^{ini} is perturbed by a randomly generated noise in the order of $\Delta c^{\text{ini}} = \pm 0.05$. A time adaptive implicit Euler backward time stepping scheme with $\theta = 1.0$ based on an initial time step size of $\Delta t = 1$ is adopted.

Remark 7 (Non-dimensionalization) The actual calculations are performed for a non-dimensional version of Eq. (11). Since RT is a constant we can pull it out of the mobility \mathbf{M} , Eq. (15), and move it into the free energy and the gradient energy. Consequently, $\partial_c^2 \Psi^{\text{con}}$ is dimensionless and κ has the units of a length squared. We chose the diffusivity D_0 and the gradient energy κ_0 as characteristic parameters. Accordingly, the resulting dimensionless versions of time and space, denoted with an asterisk, are

$$t^* = \frac{t}{\kappa_0/D_0} \quad \text{and} \quad x^* = \frac{x}{\sqrt{\kappa_0}}. \quad (35)$$

4.1 Isotropic diffusion–influence of the surface energy

In the first example, Fig. 3, we elaborate on the influence of different surface energies Ψ^{sur} at a constant configurational energy Ψ^{con} . We focus in particular on the early stages of diffusion during which phase separation is the dominant driving mechanism.

If the surface energy is deactivated all together by setting $\kappa = 0$, Fig. 3a), the problem is essentially an inverse (uphill) diffusion problem, which is known to be numerically unstable, see Lattès and Lions [14]. The result are oscillations on a node-level, which are not bounded by the reasonable concentration space between the binary mixture end-members (the colorspace in Fig. 3a is adjusted to the range between the binodes). Note, that the same phenomenon happens when the numerical resolution is not sufficient. Once the internal length scale is too small in comparison to the finite element size, the numerical results become mesh dependent. Spurious mesh dependency can thus be observed for $\kappa = 0$ due to the lack of an internal length scale. In this case the finite element simulation is entirely governed by the underlying discretization. The concentration profile is dominated

by characteristic spurious checkerboard modes. Accordingly, if the applied discretization is too coarse to resolve pattern formation appropriately, the numerical results become meaningless. The incorporation of the surface energy term of Landau–Ginzburg format is thus not only physically relevant to account for long range interaction but also mandatory from a numerical point of view.

Figs. 3b–d show the effect of increasing the surface energy. Increasing κ leads to an increased initial lamella size. Hence, the choice of the gradient energy coefficient $\kappa = \lambda^2 \gamma$ directly effects the internal length. For dimensional parameters, however, Figs. 3b–d are of equal size. Due to this effect κ also affects the progress of the unmixing, compare Figs. 3b,d. Because material has to diffuse much further in Fig. 3d than in Fig. 3b the process of unmixing is in an earlier stage and the binodes are not yet reached anywhere in the domain.

4.2 Isotropic diffusion–influence of initial concentration

Next, we focus on the influence of the mean initial concentration c^{ini} on the morphology, Fig. 4. There are essentially two different types of morphologies, particulate and co-continuous worm-like. The particulate (bubble) morphology forms when c^{ini} is close to one of the binodal values, Figs. 4a, d. If c^{ini} represents approximately equal proportions of the binodal values, cf. Fig. 4b, then worm-like structures result, which resemble the textures shown in Fig. 1a and especially Fig. 1b. In between worm-like and particulate configuration there is a transition zone around 35% of the minor phase [18] where the two morphologies are mixed such as shown in Fig. 4c. For particular shapes of the configurational free energy curve not all the morphologies may be possible. For example the white bubble model with $c^{\text{ini}} = 0.40$ is close to the lower spinode, Fig. 2. Would, for given binodes, the lower spinode be located at an even higher c value, then the white bubble morphology would become impossible because it would be situated outside the spontaneous demixing region.

There is also a remarkable difference between the sizes of individual structures that emerge when the mineral unmixes, compare for example Figs. 4a, d. The reason for this is that the initial wavelength, λ^{ini} , is related to the curvature of the configuration free energy curve by

$$\lambda^{\text{ini}} \approx \sqrt{-\frac{\kappa}{\partial_c^2 \Psi^{\text{con}}(c^{\text{ini}})}}, \quad (36)$$

see [18]. Since the curvature is smallest the example in Fig. 4a the bubble size is largest. Consequently, phase separation is slowest since the pathways are longest; gray parts of the domain did not unmix at all.

4.3 Isotropic diffusion–Ostwald ripening

Let us now focus on the temporal evolution of the concentration profile for a sufficiently large fixed internal length and a fixed initial concentration of $c^{\text{ini}} = 0.57$ situated in the unstable spinodal region. After the nuclei of the new minerals have been produced, a ripening process occurs, which is

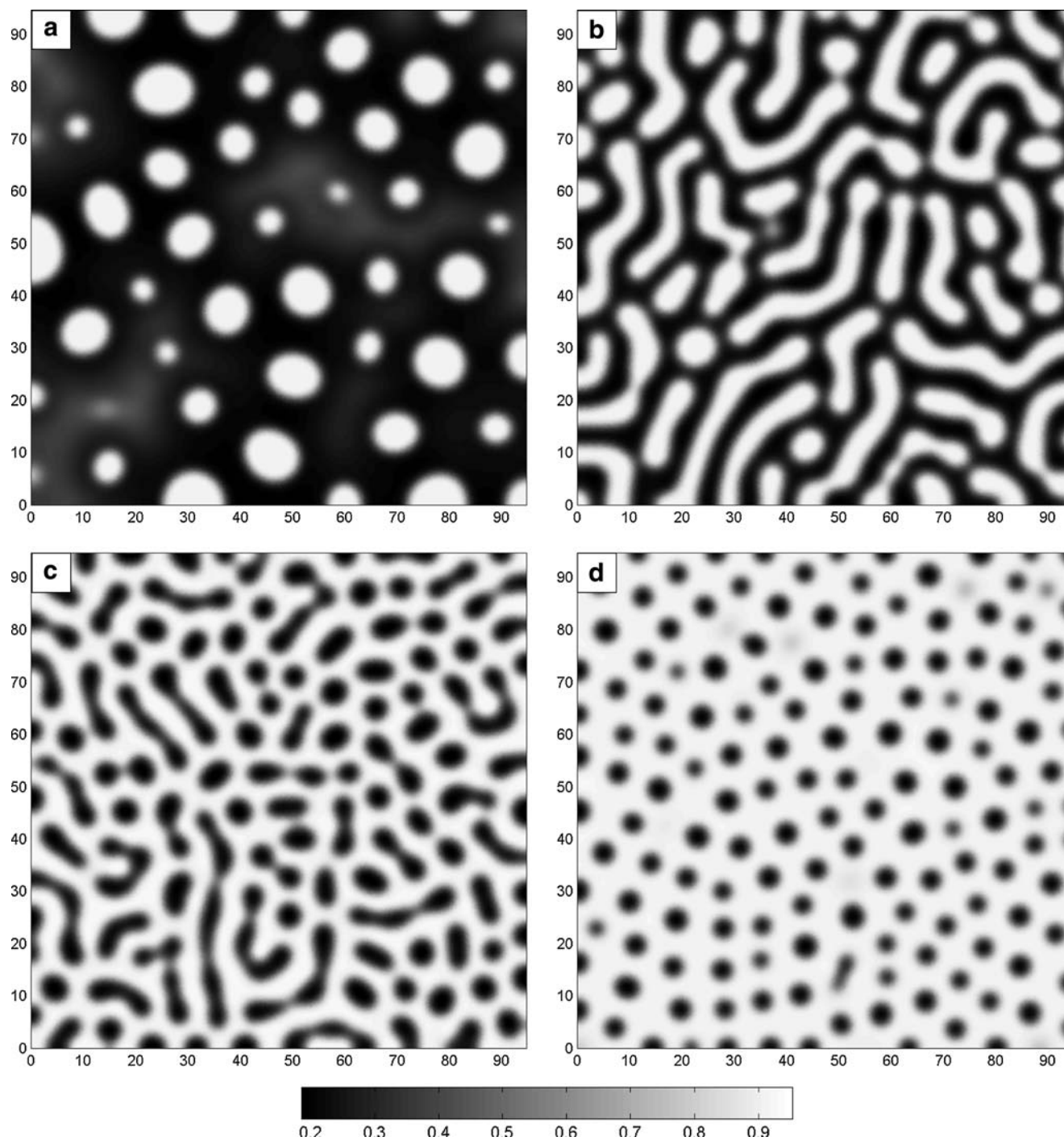


Fig. 4 Isotropic diffusion – influence of initial concentration. **a** $c^{\text{ini}} = 0.40$, $t^* = 750$, **b** $c^{\text{ini}} = 0.57$, $t^* = 111$, **c** $c^{\text{ini}} = 0.68$, $t^* = 67$, **d** $c^{\text{ini}} = 0.80$, $t^* = 111$

typically referred to as Ostwald ripening. Thereby, no new nuclei are formed, but large nuclei grow at the expense of smaller ones. Since the process of Ostwald ripening takes place at a much slower time scale, we suggest an adaptive time marching scheme and increase or decrease the time step size in response to the convergence behavior of the Newton Raphson scheme.

Figure 5 depicts the temporal evolution of the concentration fields. Obviously, two stages of diffusion can be classified: stage I is driven by minimizing the configurational energy Ψ^{con} . It basically accounts for the short term effect of the local concentrations being driven into either of the two binodes, compare Figs. 5a and b. Short wavelength components of the initial noise are de-amplified and spread and then the

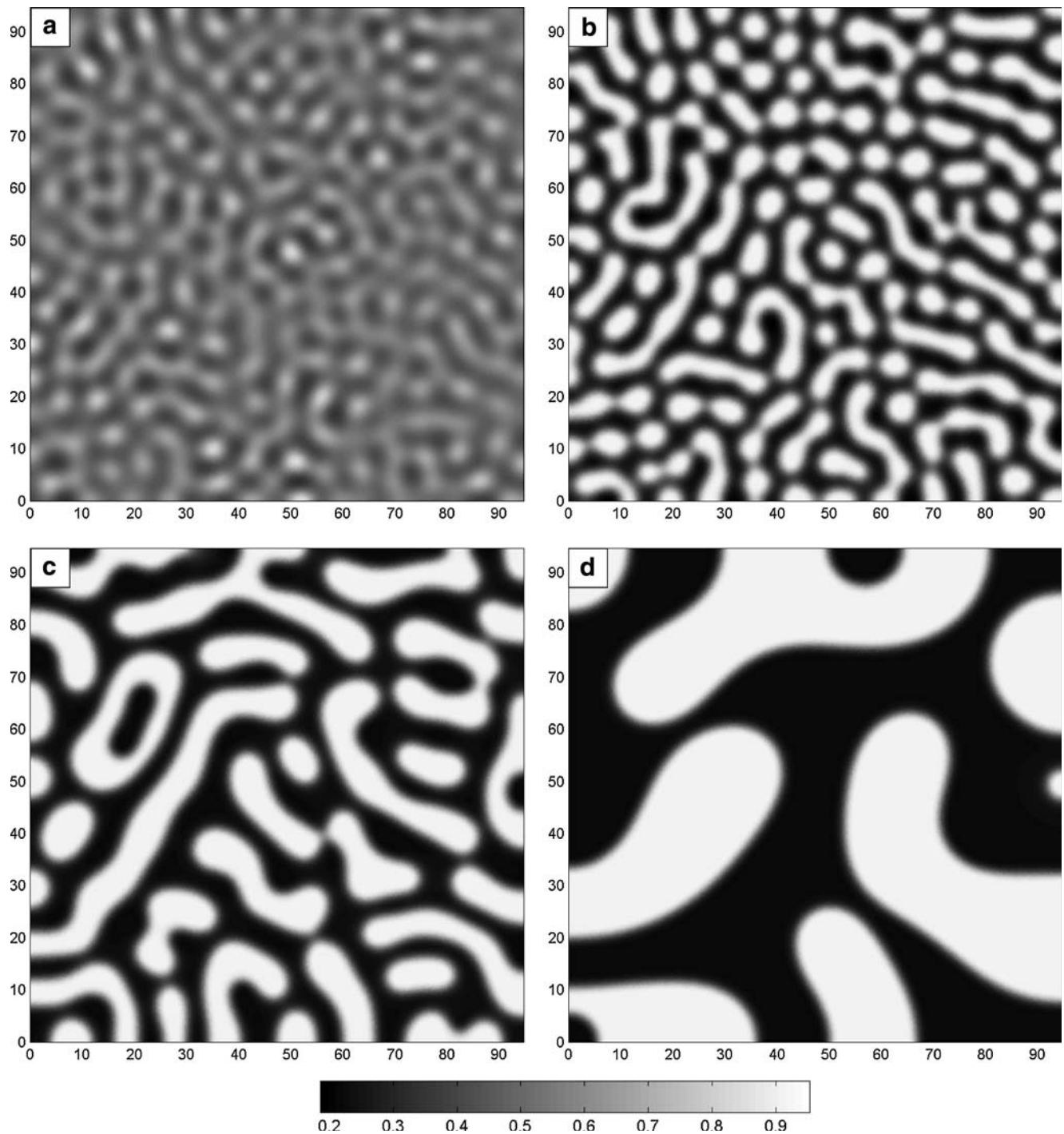


Fig. 5 Isotropic diffusion – different stages of isotropic mineral growth: phase separation and Ostwald ripening. Average system concentration is $c^{\text{ini}} = 0.57$. **a** $t^* = 25$, **b** $t^* = 56$, **c** $t^* = 252$, **d** $t^* = 8050$

fastest growing wavelength starts to develop, see [17]. Stage II is then driven by minimizing the surface energy Ψ^{sur} . As such, it accounts for long term effects of ageing, clustering, grain coarsening and Ostwald ripening. During this second stage, small crystal particles and nuclei are resorbed and their material is added to the larger crystals, compare Figs. 5c, d. The solution converges towards a stable state which finally

minimizes the sum of the configurational and surface contribution to the free energy as one single big grain is generated. The final and stable configuration for all our experiments is just a single interface between the two binodal phases. Since in Ostwald ripening the domain growth scales proportional to the cubic root of time this final stage takes a considerable amount of time to be reached.

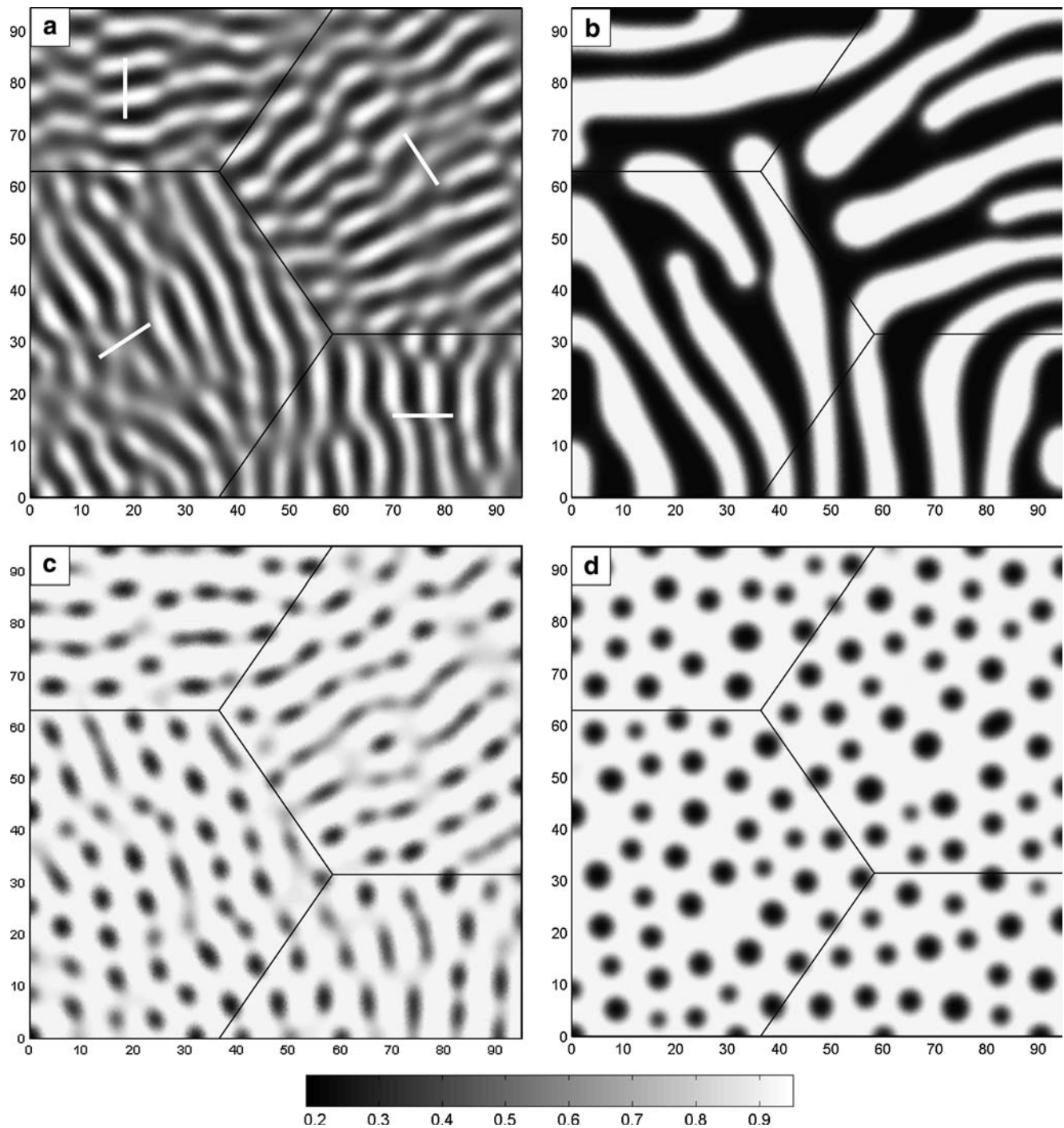


Fig. 6 Anisotropic diffusion – different stages of anisotropic mineral growth: phase separation and Ostwald ripening. The fast diffusion direction is symbolized on a) by the *white lines*. **a** $c^{\text{ini}} = 0.57$, $t^* = 36$, **b** $c^{\text{ini}} = 0.57$, $t^* = 938$, **c** $c^{\text{ini}} = 0.80$, $t^* = 95$, **d** $c^{\text{ini}} = 0.80$, $t^* = 216$

4.4 Anisotropic diffusion–mineral growth influenced by crystal lattice

Mineral unmixing frequently exhibits preferentially oriented lamellae, e.g. Fig. 1a. A possible reason for this are the often anisotropic diffusion coefficients. We investigate this effect in the two models shown in Fig. 6. The first series illustrated

in the upper Figs. 6a, b shows the evolution of morphologies with a mean initial concentration $c^{\text{ini}} = 0.57$ located in between to two binodal points. The second series in the lower Figs. 6c, d is based on an initial concentration of $c^{\text{ini}} = 0.80$ close to one of the binodal values. In both simulations, four grains (domains) are given different principal diffusion directions indicated by the white lines in Fig. 6a. Although the

principal diffusion values differ only by a factor two, both models are clearly affected by the anisotropy and show preferential morphology orientation. Note, that the preferential morphology orientation is orthogonal to the fast diffusion direction. For usually worm-like morphologies, cf. Fig. 4b, the anisotropy of the diffusion coefficients prevails in the morphology until late stages of ripening, Fig. 6b. For usually bubble-like morphologies, cf. Fig. 4d, the anisotropy of the diffusion can only affect the unmixing phase; during the later ripening stages the surface tension is too strong and forces the isotropic picture to develop, Fig. 6d. Henceforth, there is a competition between the anisotropy of the diffusion and the surface energy minimization.

Note that the required thermodynamical data that characterizes anisotropic diffusion appropriately is not always readily available. Based on the arguments outlined by Putnis [21], we have assumed that diffusion in the characteristic direction is twice as fast. In future investigations, inverse analyses could possibly be used to provide further insight into the additional parameters of anisotropy.

Let us finally give a dimensional example of the rather successful preferential lamellae producing model shown in Figs. 6a, b. Realistic values for the fast diffusion and the RT normalized gradient energy are $10^{-23} m^{-2}/s$ and $10^{-17} m^{-2}$, respectively. The gradient energy coefficient has been determined with the help of Eq. (2.15) in Cahn and Hilliard [4], evaluated for the particular shape of the free energy function as illustrated in Fig. 2 in combination with a surface tension of $0.0643 J/m^{-2}$ taken from the literature, see also Eq. (7.1) in Nauman and He [18]. We can then use Eq. (35) to convert the nondimensional space and time of the model in Figs. 6a, b into dimensional units. The resulting domain size is $300 nm$ and the elapsed times are approximately 1 year for Fig. 6a and 30 years for Fig. 6b. The lamellae shown in Fig. 1 are therefore substantially larger than the ones that this model produced in the given time interval. Hence, the lamellae in the natural example must have had much more time to ripen. Provided that the required material parameters of the end-members of the exsolution process are known, the developed numerical model can therefore not only be used to study unmixing, ripening and morphology patterns and evolution, but also to decipher important parameters from natural minerals such as residence times at certain conditions, which are crucial for interpreting the geological history of a region.

5 Discussion

A stable, robust and efficient simulation tool for the computational modeling of spinodal decomposition and related phenomena has been presented. It is governed by a nonlinear diffusion equation for non-ideal mixtures supplemented by a surface energy term of Landau–Ginzburg type. The latter typically introduces computationally cumbersome fourth order gradients of the order parameter. In order to avoid higher order continuity requirements within the finite element discretization, the governing fourth order equation was substi-

tuted by two second order equations introducing the local and the nonlocal concentration field as primary unknowns.

The derived formulation is capable of predicting the formation of both particulate as well as co-continuous worm-like microstructures in response to different initial concentrations. It is not only able to capture the early stages of phase separation but also to predict the later stages of Ostwald ripening. Efficient long terms simulations have been enabled by the application of a heuristic but rather powerful adaptive time stepping scheme in which the time step size has been adapted continuously in response to the current convergence behavior of the Newton iteration.

In contrast to the literature which is dominated by spectral codes and finite different schemes, a finite element based discretization technique has been adopted. It allows for the simulation of arbitrarily shaped domains and is not confined to periodic boundary conditions. Moreover, the additional incorporation of deformation dependent growth phenomena is straightforward in the finite element context. In particular in combination with crystallographic anisotropy and large deformations, a finite element discretization might be superior to existing finite difference schemes.

The developed finite element based simulation tool has been tested in the context of isotropic and anisotropic mineral unmixing and growth. The documented simulations are believed to provide further insight into driving processes of complex geologically phenomena that are observable in nature. However, the presented simulation tool is not restricted to geological phenomena alone. It can equally well be applied to many technically relevant processes such as, e.g., the microstructure evolution of solder alloys, and is thus believed to be extremely powerful.

Acknowledgements We would like to thank Bjørn Jamtveit for providing the thin sections shown in Fig. 1. Rainer Abart, James Connolly, Krishna Garikipati, Else-Ragnhild Neumann, Yuri Podladchikov, Nina Simon, and Garth Wells are thanked for fruitful discussions.

References

1. Aramovich CJ, Herd CDK, Papike JJ (2002) Symplectites derived from metastable phases in martian basaltic meteorites. *Am Mineral* 87:1351–1359
2. Asaro RJ, Tiller WA (1972) Interface morphology development during stress corrosion cracking: Part I. Via surface diffusion. *Metallurg Trans* 3:1789–1796
3. Cahn JW (1959) Free energy of a non-uniform system. II. Thermodynamic basis. *J Chem Phys* 30:1121–1124
4. Cahn JW, Hilliard JE (1958) Free energy of a non-uniform system. I. Interfacial free energy. *J Chem Phys* 28:258–267
5. Cahn JW, Hilliard JE (1959) Free energy of a non-uniform system. III. Nucleation in a two-component incompressible fluid. *J Chem Phys* 31:688–699
6. Flory PJ (1942) Thermodynamics of high polymer solutions. *J Chem Phys* 10:51–61
7. Golla-Schindler U, O'Neill HSC, Putnis A (2005) Direct observation of spinodal decomposition in the magnetite-hercynite system by susceptibility measurements and transmission electron microscopy. *Am Mineral* 90:1278–1283
8. Gurtin ME (1996) Generalized Ginzburg-Landau and Cahn-Hilliard equations based on a microforce balance. *Physica D* 92:178–192

9. Hovis GL, Kroll H, Breit U, Richard AY (2003) Elastic strain enthalpies of exsolution: HF solution calorimetric experiments on alkali aluminosilicate and aluminogermanate feldspars. *Am Mineral* 88:547–555
10. Huggins ML (1942) Theory of solutions of high polymers. *J Am Chem Soc* 64:1712–1719
11. Lally JS, Heuer AH, Nord GL, Christie JM (1975) Subsolidus reactions in lunar pyroxenes – electron petrographic study. *Contrib Mineral Petrol* 51:263–281
12. Langer JS (1971) Theory of spinodal decomposition in alloys. *Ann phys* 65:53–86
13. Larché F, Cahn JW (1973) A linear theory of thermochemical equilibrium of solids under stress. *Acta Metall* 21:1051–1063
14. Lattès R, Lions J-L (1969) The method of quasireversibility applications to partial differential equations. Elsevier, Amsterdam
15. Lifshitz IM, Slyozov VV (1961) The kinetics of precipitation from supersaturated solid solutions. *J Phys Chem Solids* 19:35–50
16. McCallister RH (1978) The coarsening kinetics associated with exsolution in an iron-free clinopyroxene. *Contrib Mineral Petrol* 65:327–331
17. Nauman EB, Balsara NP (1988) Spatially local minimizers of the Landau-Ginzburg functional. *Q Appl Math* 46:375–379
18. Nauman BE, He DQ (2001) Nonlinear diffusion and phase separation. *Chemical Engineering Science* 56:1999–2018
19. Novick-Cohen A, Segel LA (1984) Nonlinear aspects of the Cahn-Hilliard equation. *Physica D* 10:277–298
20. Ostwald W (1900) Über die vermeintliche Isometrie des roten und gelben Quecksilberoxyds und die Oberflächenspannung fester Körper. *Z Phys Chem* 6:495–503
21. Putnis A (1992) Introduction to mineral sciences. Cambridge University Press, London
22. Srolovitz DJ (1989) Surface morphology evolution in stressed solids: Surface diffusion controlled crack initiation. *Acta Metall* 37:621–625
23. Ubachs RLJM, Schreurs PJG, Geers MGD (2004) A nonlocal diffuse interface model for microstructure evolution in tin-lead solder. *J Mech Phys Solids* 52:1763–1792
24. Ubachs RLJM, Schreurs PJG, Geers MGD (2005) Phase field dependent viscoplastic behaviour of solder alloys. *Int J Solids Struct* 42:2533–2558
25. Vernon RH (2004) A practical guide to rock microstructure. Cambridge University Press, London
26. Vollmayr-Lee BP, Rutenberg AD (2003) Fast and accurate coarsening simulation with an unconditionally stable time step. *Phys Rev E* 68:66703
27. van der Waals JD (1893) Thermodynamische Theorie der Kapillarität unter Voraussetzung stetiger Dichteänderung. *Z Phys Chem* 13:675–725
28. Wagner C (1961) Theorie der Alterung von Niederschlägen durch Umlösen (Ostwald-Reifung). *Z Elektrochem* 65:581–591
29. Waldbaum DR, Thompson JB (1969) Mixing properties of sanidine crystalline solutions. Phase diagrams from equations of state. *Am Mineral* 54:1274–1298
30. Wells GN, Kuhl E, Garikipati K (2006) A discontinuous Galerkin method for the Cahn-Hilliard equation. Accepted for publication in *J. Comput. PHYS.*